Nanoscale

Crossover between rigid and reconstructed moiré lattice in *h*-BN-encapsulated twisted bilayer WSe_2 with different twist angles

Journal:	*Nanoscale*
Manuscript ID	NR-ART-04-2024-001863.R1
Article Type:	Paper
Date Submitted by the Author:	14-May-2024

Complete List of Authors:	Kinoshita, Kei; The University of Tokyo Institute of Industrial Science Lin, Yung-Chang ; National Institute of Advanced Industrial Science and Technology Tsukuba Moriya, Rai; The University of Tokyo Institute of Industrial Science Okazaki, Shota; Tokyo Institute of Technology Laboratory for Materials and Structures Onodera, Momoko; The University of Tokyo Institute of Industrial Science Zhang, Yijin; The University of Tokyo Institute of Industrial Science Senga, Ryosuke; National Institute of Advanced Industrial Science and Technology Tsukuba Watanabe, Kenji; NIMS Taniguchi, Takashi; NIMS Sasagawa, Takao ; Tokyo Institute of Technology Laboratory for Materials and Structures Suenaga, Kazu; Osaka University, The Institute of Scientific and Industrial Research (ISIR-SANKEN) Machida, Tomoki; The University of Tokyo Institute of Industrial Science, Institute of Industrial Science

SCHOLARONE™
Manuscripts

Crossover between rigid and reconstructed moiré lattice in *h*-BN-encapsulated twisted bilayer WSe_2 with different twist angles

Kei Kinoshita[1,*], Yung-Chang Lin[2], Rai Moriya[1,*], Shota Okazaki[3], Momoko Onodera[1], Yijin Zhang[1], Ryosuke Senga[2], Kenji Watanabe[4], Takashi Taniguchi[5], Takao Sasagawa[3], Kazu Suenaga[6], and Tomoki Machida[1,*]

[1] *Institute of Industrial Science, University of Tokyo, 4-6-1 Komaba, Meguro, Tokyo 153-8505, Japan*

[2] *National Institute of Advanced Industrial Science and Technology, 1-1-1 Higashi, Tsukuba 305-8565, Japan*

[3] *Laboratory for Materials and Structures, Tokyo Institute of Technology, 4259 Nagatsuta, Yokohama, Kanagawa 226-8503, Japan*

[4] *Research Center for Electronic and Optical Materials, National Institute for Materials Science, 1-1 Namiki, Tsukuba 305-0044, Japan*

[5] *Research Center for Materials Nanoarchitectonics, National Institute for Materials Science, 1-1 Namiki, Tsukuba 305-0044, Japan*

[6] *The Institute of Scientific and Industrial Research, Osaka University, 8-1 Mihogaoka, Ibaraki, Osaka 567-0047, Japan*

---

*E-mail: kkino@iis.u-tokyo.ac.jp; moriyar@iis.u-tokyo.ac.jp; tmachida@iis.u-tokyo.ac.jp

A moiré lattice in a twisted-bilayer transition metal dichalcogenide (tBL-TMD) exhibits a complex atomic reconstruction effect when its twist angle is less than a few degrees. The influence of the atomic reconstruction on material properties of the tBL-TMD has been of particular interest. In this study, we performed scanning transmission electron microscopy (STEM) imaging of a moiré lattice in *h*-BN-encapsulated twisted bilayer WSe_2 with various twist angles. Atomic-resolution imaging of the moiré lattice revealed a reconstructed moiré lattice below a crossover twist angle of ~4° and a rigid moiré lattice above this angle. Our findings indicate that *h*-BN encapsulation has a considerable influence on lattice reconstruction, as the crossover twist angle was larger in *h*-BN-encapsulated devices compared to non-encapsulated devices. We believe that this difference is due to the improved flatness and uniformity of the twisted bilayers with *h*-BN encapsulation. Our results provide a foundation for a deeper understanding of the lattice reconstruction in twisted TMD materials with *h*-BN encapsulation.

Introduction

Two-dimensional (2D) materials can be stacked using van der Waals (vdW) forces. The difference in the in-plane crystal orientations between adjacent layers, known as the twist angle, significantly modifies the properties of the stacked 2D materials. A ground-breaking discovery was made by constructing small-angle twisted bilayer graphene and transition metal dichalcogenides (TMDs). To date, correlated insulators [1, 2], superconductivity [3], Chern insulators [4-7], interlayer excitons [8-11], and ferroelectricity [12, 13] have been demonstrated and received considerable attention in the twisted bilayer system. These phenomena are owing to the presence of long-period moiré superlattice potential created by the small-angle twist. Thus, the use of moiré lattices has become increasingly important in the field of 2D materials.

The local structure of moiré lattice was investigated using various imaging methods, including transmission electron microscopy (TEM), conductive atomic force microscopy (c-AFM), piezoresponse force microscopy (PFM), and scanning tunneling microscopy (STM) [14-25]. These investigations unveiled that the actual moiré lattice in the small-angle twisted bilayers undergoes relaxation, leading to the transformation of a reconstructed moiré lattice. In Fig. 1, we consider the lattice structure for twisted-bilayer WSe_2 (tBL-WSe_2) as a representative twisted-bilayer transition metal dichalcogenide (tBL-TMD). Two monolayers of WSe_2 (ML-WSe_2) are stacked with a twist angle θ_{BL} of a few degrees (Fig. 1a). Here, we define $\theta_{BL} = 0°$ as the in-plane orientation of the two aligned ML-WSe_2, similarly to 3R-stacking. The twist between the hexagonal lattice of two ML-WSe_2 generates a moiré pattern as shown in Fig. 1b. The moiré pattern depicted in Fig. 1b is characterized as a rigid moiré lattice, signifying that the atoms in each ML-

WSe_2 remain undisplaced following their vertical stacking with a twist angle. This configuration is further schematically represented in Fig. 1c, where the three principal stacking configurations are differentiated by varying colors. At the location marked by an orange filled circle at the center of each hexagonal pattern, the Se and W atoms in the upper and lower ML-WSe_2 are vertically aligned, as shown in the left panel of Fig. 1d. This arrangement is termed as Se/Se (W/W) stacking. Conversely, at the positions indicated by the blue and light blue circles at the vertices of the hexagon, the W (Se) atoms of the upper ML-WSe_2 layer are positioned directly above the Se (W) atoms of the lower ML-WSe_2 layer, as illustrated in the middle and right panels of Fig. 1d. These configurations are designated as W/Se (Se/W) stacking.

Using this schematic illustration provided, the lattice reconstruction process can be elucidated as follows (further details are available in the Supporting Information, Fig. S1). When the θ_{BL} is large, a rigid moiré pattern is observed (Fig. 1c and top left panel of Fig. S1). As θ_{BL} progressively decreases, the moiré period lengthens (illustrated from the top left to the bottom left panels in Fig. S1). Concurrently, the areas characterized by W/Se and Se/W stacking expand (from the left to right column in Fig. S1). At reduced θ_{BL} values, the W/Se and Se/W stacking domains further enlarge and transform into a triangular shape to occupy the area bounded by the Se/Se stacking regions (marked by orange solid circles) and the boundary regions between the W/Se and Se/W domains (shown in the right column of Fig. S1). This configuration represents the reconstructed moiré lattice. The reconstruction process aims to minimize the total energy, E_{total}, of tBL-WSe_2, which is expressed as $E_{total} = E_{inter} + E_{intra}$, where E_{inter} represents the interlayer stacking energy and E_{intra} the intralayer strain energy [26, 27]. As W/Se (Se/W) stacking

configurations are the most energetically favorable, expanding these areas reduces the first energy term, thereby facilitating the reconstruction process. However, this expansion also introduces strain within the lattice, increasing the second energy term. Consequently, the extent of reconstruction is determined by the balance between these two energy contributions, making it dependent on the twist angle. Therefore, with decreasing twist angles, both an increase in the moiré period and an enhancement in reconstruction are observed simultaneously, leading to transformation of the pattern from Fig. 1c to 1e and then subsequently to Fig. 1f.

Thus, atomic reconstruction emerges as a fundamental characteristic of moiré lattices in small-angle twisted bilayers of 2D materials. Nevertheless, systematic examinations regarding crossover between rigid and reconstructed moiré lattices in twisted bilayers remain scarce. Additionally, we observed a notable discrepancy between the device architectures used for moiré pattern observations and those employed to study electron correlation phenomena in twisted bilayers. Historically, investigations of moiré lattice have primarily focused on non-encapsulated twisted bilayers, which are either fully exposed or supported solely at a single interface due to experimental constraints. In contrast, the exotic electron-correlation phenomena previously mentioned were predominantly detected in *h*-BN-encapsulated twisted bilayers. This highlights the need for a comprehensive investigation into the role of *h*-BN encapsulation. In this study, we conducted scanning transmission electron microscopy (STEM) observations of atomic reconstruction in twisted bilayer WSe_2 (tBL-WSe_2) across various twist angles and under different *h*-BN encapsulation conditions.

Experimental

The structure configuration (side view) and a low-magnification STEM image (top view) of the fabricated *h*-BN/tBL-WSe_2/*h*-BN vdW heterostructure are depicted in Figs. 1g and 1h, respectively. The stacking of the heterostructures was performed by a pick-up method using polycarbonate (PC) [28, 29]. *h*-BN flakes with thicknesses ranging from 5 to 7 nm were selected. The twist angle of tBL-WSe_2 was controlled through the cut-and-stack method, which involves laser precutting of ML-WSe_2 (see Supporting Information, Fig. S2, for detailed information on device fabrication) [30, 31]. The heterostructure was initially constructed on an SiO_2/Si substrate. Subsequently, the sample was transferred onto a TEM grid (Quantifoil 4220C) [32]. The heterostructure overlapping the holes in the grids was observed by atomic resolution STEM imaging with an electron beam acceleration voltage of 60 kV.

Results and discussion

Figs. 1i−k show higher magnification STEM images of *h*-BN-encapsulated tBL-WSe_2 for different twist angles: θ_{BL} = 5.3°, 3.6°, and 2.9°. The θ_{BL} values were ascertained by analyzing the fast Fourier transform (FFT) patterns of the corresponding STEM images. For all the samples, high-contrast STEM images were obtained, enabling precise analysis of the moiré lattice structures in tBL-WSe_2. At θ_{BL} = 5.3°, the STEM image exhibited a hexagonal periodic pattern (Fig. 1i), consistent with that of a rigid moiré lattice as depicted in Fig. 1b, where the positions of the Se/Se stacking regions are indicated by orange circles. Conversely, at a reduced twist angle of θ_{BL} = 3.6°, the lattice

period increased and the hexagonal pattern became less distinct (Fig. 1j). This pattern aligns with the lattice structure illustrated in Fig. 1e, where the W/Se (Se/W) regions expand to fill the spaces between the Se/Se regions (see Supporting Information, Fig. S3, for detailed STEM image analysis). Consequently, the moiré lattice of tBL-WSe_2 undergoes partial reconstruction at θ_{BL} = 3.6°. With a further reduction in θ_{BL} to 2.9°, triangular patterns emerged in the STEM images (Fig. 1k), attributed to the further expansion of the W/Se (Se/W) domains into a triangular domain structure, delineating clear boundary regions between the domains as shown in Fig. 1f. Thus, the STEM lattice image for θ_{BL} = 2.9° represents a fully reconstructed moiré lattice. These observations underscore that the moiré patterns in tBL-WSe_2 exhibit a significant dependence on the twist angle.

Next, we determined the crossover θ_{BL} between the reconstructed and rigid moiré patterns by analyzing STEM images of *h*-BN-encapsulated tBL-WSe_2 across varying θ_{BL}. Atomic reconstruction is depicted in Fig. 2a, showing the expansion of the W/Se and Se/W domains from the vertices of the hexagonal moiré unit cell (outlined in green), while the non-reconstructed region centered around the Se/Se stacking (outlined in purple) diminishes. The degree of atomic reconstruction is quantified by the ratio of the area of the non-reconstructed region, S_{center}, to the total area of the moiré unit cell, $S_{moiré}$ (purple hexagon). The outlines of the green and purple hexagons are determined graphically from the TEM images (See Supporting Information, Fig. S3). A smaller $S_{center}/S_{moiré}$ ratio indicates a higher degree of atomic reconstruction. Results from the tBL-WSe_2 samples at various θ_{BL} values are displayed in Fig. 2b, with enlarged versions available in Fig. S3 of the Supporting Information. The $S_{center}/S_{moiré}$ ratio varies with θ_{BL},

and this relationship is graphically represented in Fig. 2c. Notably, the $S_{center}/S_{moiré}$ ratio monotonically increases from θ_{BL} = 2.4° (the smallest twist angle investigated) to approximately θ_{BL} ~ 4.0°. Beyond this point, the slope of the $S_{center}/S_{moiré}$ ratio versus θ_{BL} decreases, nearing a plateau. From these analyses, we establish that θ_{BL} ~ 4.0° marks a definitive boundary below which progressive atomic reconstruction of the moiré lattice is observed. Consequently, we have identified θ_{BL} ~ 4° as the crossover twist angle between reconstructed and rigid moiré lattices. We note that there was no apparent lattice deformation in the TEM images above the crossover θ_{BL}, as observed in the heterobilayer system [33], and we believe that tBL-WSe_2 forms a nearly ideal rigid lattice in this region.

We further explore the impact of *h*-BN encapsulation on the atomic reconstruction of tBL-WSe_2. We compared the crossover twist angles distinguishing the rigid and reconstructed moiré patterns across three different sample structures: 1) tBL-WSe_2 fully encapsulated with *h*-BN, 2) tBL-WSe_2 topped with an *h*-BN capping layer, and 3) non-encapsulated tBL-WSe_2, as depicted in Figs. 3a−c, respectively. Each structure was suspended in the apertures of the TEM grid, facilitating observation. The twist-angle-dependent behavior observed in the STEM images for each structure is presented in Figs. 3d−f. For the fully *h*-BN-encapsulated structure, atomic reconstruction was consistently observed between θ_{BL} = 2.4° and 3.8° (Fig. 3d and Fig. S3). As noted previously, the crossover twist angle for this structure was established at approximately θ_{BL} ~ 4°. For the sample with an *h*-BN capping layer, atomic reconstruction manifested at θ_{BL} = 2°, 2.9°, and 3.3°, identifiable by the emergence of triangular pattern, while it was absent at θ_{BL} = 3.6° and 4.2° (Fig. 3e). Hence, the crossover angle for this structure lies between 3.3° and 3.6°. In the case of the non-encapsulated tBL-WSe_2, triangular patterns were sporadically

visible at θ_{BL} = 0.5° and 2.1°; however, the periodicity was challenging to discern at lower twist angles (Fig. 3f). For θ_{BL} = 3.1°, 3.5°, and 5.9°, there was no indication of the reconstructed moiré pattern, placing the crossover angle between 2.1° and 3.1°. The crossover angle for tBL-WSe_2 without *h*-BN is similar to that reported in previous studies [16, 34]. The variability in the crossover θ_{BL} for the three types of structures is more pronounced when comparing STEM images at smaller twist angles: θ_{BL} = 2.9° in Fig. 3d, θ_{BL} = 2.9° in Fig. 3e, and θ_{BL} = 3.1° in Fig. 3f, with a detailed side-by-side comparison presented in Supporting Information Fig. S4. A clear triangular reconstructed pattern is observable at θ_{BL} = 2.9° in Fig. 3d, whereas the triangular shape is less distinct at the same twist angle in Fig. 3e, and completely absent at θ_{BL} = 3.1° in Fig. 3f. A summary of the crossover between reconstructed and rigid moiré lattice for different twist angles and encapsulation is showcased in Fig. 3g. The determined lattice structures (rigid or reconstructed) are indicated by different colors, as illustrated on the right-hand side of the figure. Our findings indicate that the crossover twist angle between reconstructed and rigid moiré lattices increases in the order: (*h*-BN-encapsulated tBL-WSe_2) > (*h*-BN-capped tBL-WSe_2) > (non-encapsulated tBL-WSe_2). Therefore, it appears that the interface between *h*-BN and tBL-WSe_2 plays a crucial role in stabilizing the atomic reconstruction of tBL-WSe_2.

h-BN is recognized for its function as an atomically flat insulating substrate or tunnel barrier in devices constructed from 2D material devices [35-39]. Employing *h*-BN in the tBL-WSe_2/*h*-BN heterostructure or within the fully encapsulated *h*-BN/tBL-WSe_2/*h*-BN configuration enhances the flatness and uniformity of tBL-WSe_2 layers. It has been

recently reported that the out-of-plane distortion of Se/Se (W/W) stacking in tBL-WSe_2 is suppressed in the *h*-BN-encapsulated structure [17]. We postulate that the flat surface provided by *h*-BN-encapsulated tBL-WSe_2 reduces the interlayer spacing compared to configurations without *h*-BN; which serves as a key factor for atomic reconstruction [17, 18, 40, 41]. As discussed in Fig. 1, reconstruction aims to minimize the total energy of tBL-WSe_2, the sum of E_{inter} and E_{intra}. The distribution between these two energy contributions can be influenced by the interlayer spacing. Thus, the reconstruction in *h*-BN-encapsulated samples is more pronounced than in those without *h*-BN, also manifesting a larger crossover twist angle.

Finally, it is noteworthy that our findings demonstrate that *h*-BN encapsulation significantly enhances high-resolution STEM imaging. A comparative analysis of STEM images of the *h*-BN-encapsulated and non-encapsulated tBL-WSe_2 samples is presented in Fig. 4. The *h*-BN-encapsulated tBL-WSe_2 displayed atomic-scale resolution images of the reconstructed moiré lattices, whereas the image resolution was compromised in non-encapsulated samples. tBL-WSe_2 layers without *h*-BN encapsulation were fully suspended in the apertures of the TEM grid, resulting in natural out-of-plane corrugation and a nonuniform structure. We also observed that these suspended tBL-WSe_2 exhibit instability in their lattice structure during STEM observation, which is detailed in Supporting Information, Fig. S5. Additionally, surface contamination on non-encapsulated tBL-WSe_2 was evident, further degrading the STEM imaging quality. The considerable advantages of *h*-BN encapsulation include achieving atomic flatness in 2D materials and reducing surface impurities, which significantly enhance the precision in focusing on the target layer. Typically, it is preferable to examine the atomic structure of

2D materials when they are at their minimum thickness and free from extraneous materials above and below. Particularly, amorphous adsorbates contribute to non-crystalline contrast, which can lead to image blurring. Furthermore, the presence of overlapping crystalline materials can complicated the imaging of the target material, potentially resulting in the formation of superstructures or moiré fringes in the resulting STEM images. This effect is clearly demonstrated in Fig. S6, which presents images of WSe_2 with and without *h*-BN coverage. To minimize interference from the capping *h*-BN crystal in the images, we meticulously selected thin *h*-BN flakes with a nominal thickness of approximately 5 nm. This careful selection ensures the preservation of surface flatness integrity and to minimize its influence on the annular dark-field (ADF) contrast. By providing a flattening effect and an ultra-clean surface, we contend that *h*-BN encapsulation is an effective methodology for maintaining structural integrity and achieving high-resolution STEM characterization.

Conclusions

In summary, we conducted STEM observations on small-angle twisted bilayer WSe_2 with various *h*-BN encapsulation configurations. By measuring devices having different twist angles, we observed a crossover between a reconstructed and rigid moiré lattice. Furthermore, the observed crossover twist angle of 4° in the *h*-BN-encapsulated devices was larger than that in the non-encapsulated devices. The results shown here indicate that the presence of the *h*-BN/tBL-WSe_2 interface stabilizes the atomic reconstruction of tBL-WSe_2 compared with that without the interface. Furthermore, we

found that *h*-BN encapsulation considerably improved the resolution of the TEM images. Our results revealed the importance of *h*-BN encapsulation for atomic reconstruction in twisted TMDs and their TEM observations.

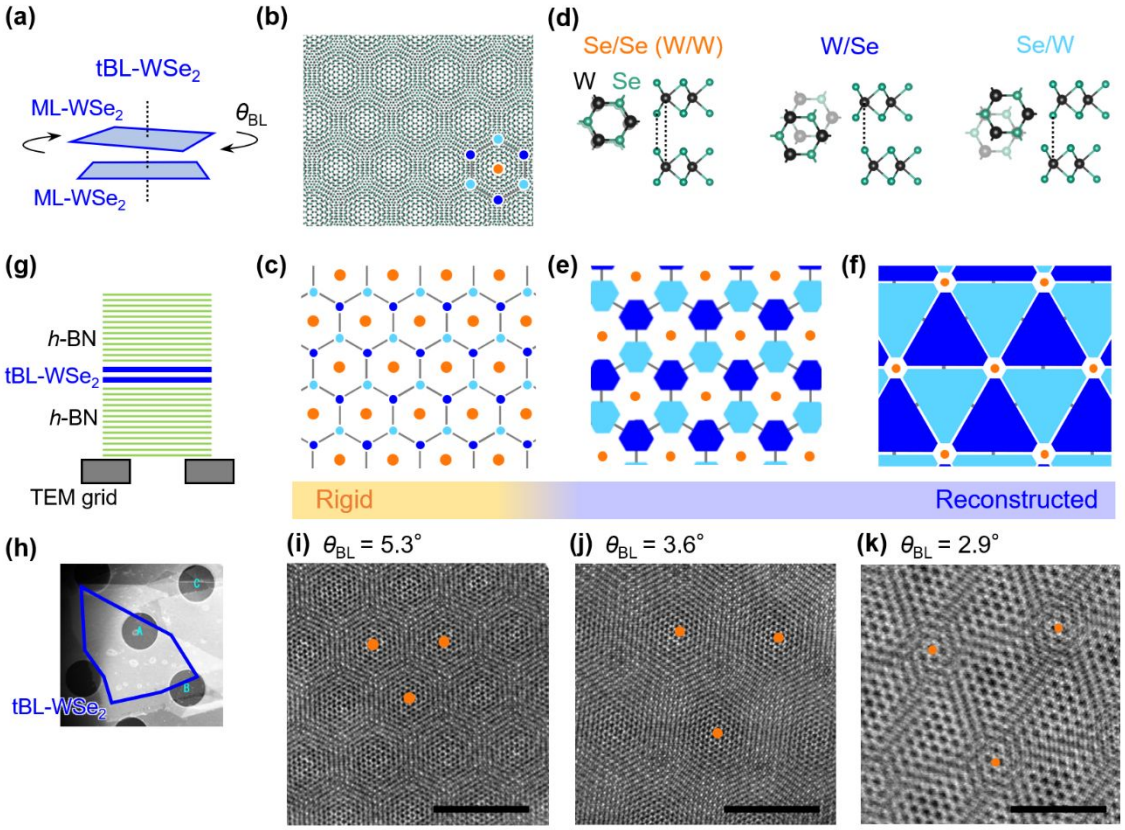

Fig. 1 (a) Schematic of stacking monolayer WSe_2 (ML-WSe_2) with twist angle θ_{BL} to fabricate twisted-bilayer WSe_2 (tBL-WSe_2). (b) Crystal structure of tBL-WSe_2 based on the crystal structure of ML-WSe_2 generated by VESTA [42]. (c) Rigid moiré pattern in tBL-WSe_2. The blue, light blue, and orange circles correspond to the locations of the local stacking for W/Se, Se/W, and Se/Se, respectively. (d) Schematics of the cross-section of W/Se, Se/W, and Se/Se stacking. (e,f) Illustration of (e) partially reconstructed moiré pattern and (f) fully reconstructed moiré pattern. (g) Schematic of the cross-section of the fabricated sample structure. The *h*-BN-encapsulated tBL-WSe_2 was placed on a TEM grid. (h) Low-magnification STEM image of the sample. (i-k) High-magnification STEM images of *h*-BN-encapsulated tBL-WSe_2 with θ_{BL} values of (i) 5.3°, (j) 3.6°, and (k) 2.9°.

The positions of the Se/Se stacking region are indicated by orange circles in each image. All scale bars are 5 nm.

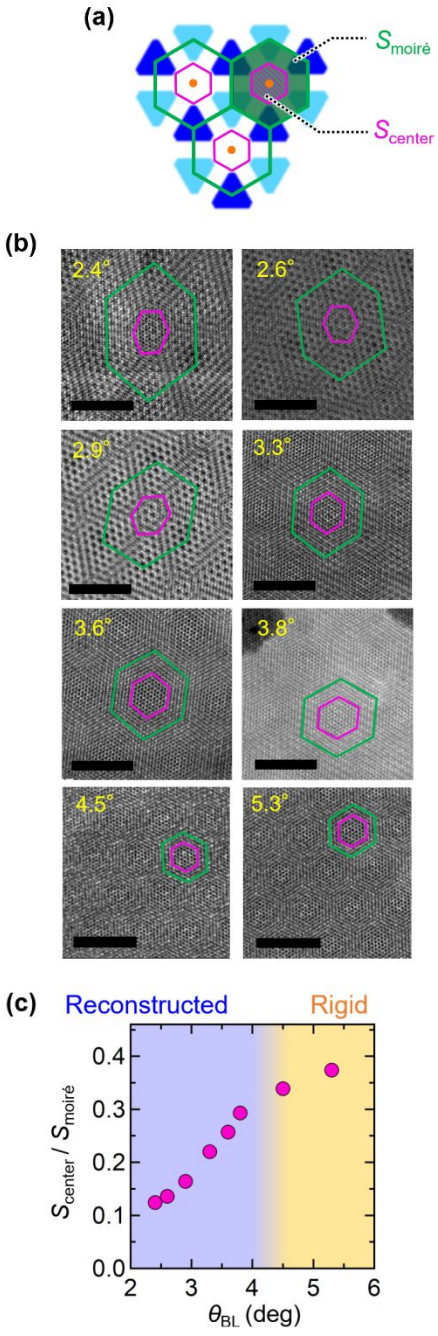

Fig. 2 (a) Illustration of reconstructed moiré lattice in tBL-WSe_2. A moiré unit cell is outlined by the green solid line, and the non-reconstructed region centered on the Se/Se stacking region is outlined by the purple solid line. (b) STEM images of tBL-WSe_2 at different twist angles. The green and purple outlines are the same as those discussed in (a). All scale bars are 5 nm. (c) Area ratio between non-reconstructed region (outlined in purple) and moiré unit cell (outlined in green) in panel (b), as a function of the twist angle θ_{BL}.

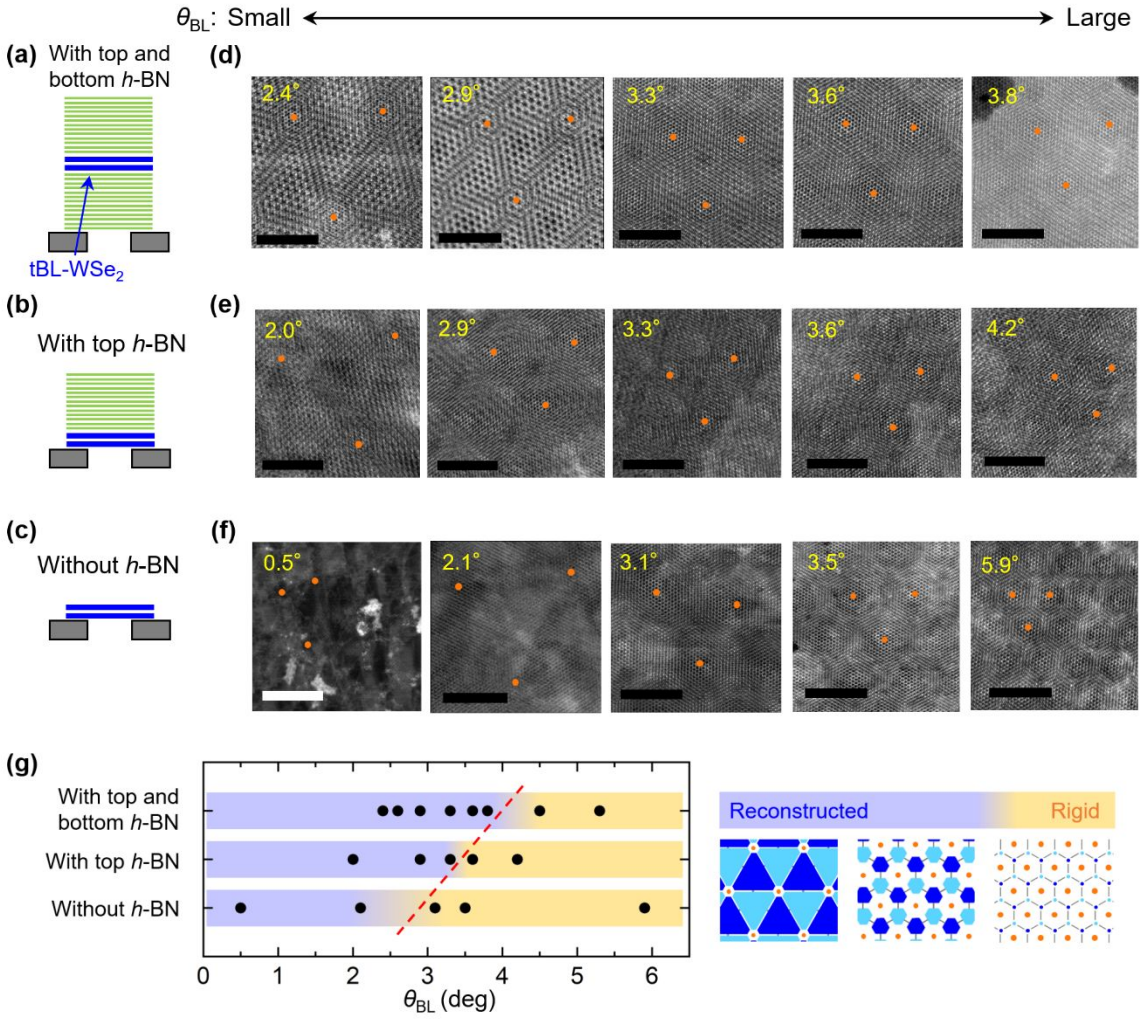

Fig. 3 (a,b,c) Illustrations of the tBL-WSe_2 device structures: (a) tBL-WSe_2 encapsulated with top and bottom h-BN, (b) tBL-WSe_2 capped with top *h*-BN, and (c) non-encapsulated tBL-WSe_2. (d,e,f) STEM images of tBL-WSe_2 with respect to different twist angles obtained for three different structures: (d) tBL-WSe_2 encapsulated with top and bottom *h*-BN, (e) tBL-WSe_2 capped with top *h*-BN, and (f) non-encapsulated tBL-WSe_2. All black scale bars are 5 nm, and a white scale bar in θ_{BL} = 0.5° of (f) is 50 nm. The positions of the Se/Se stacking region are indicated by orange circles in each image. (g) (left) Summary of the crossover between the reconstructed and rigid moiré lattice patterns for different device structures. (right) Illustration of reconstructed to rigid moiré patterns along with the color bar in the left figure.

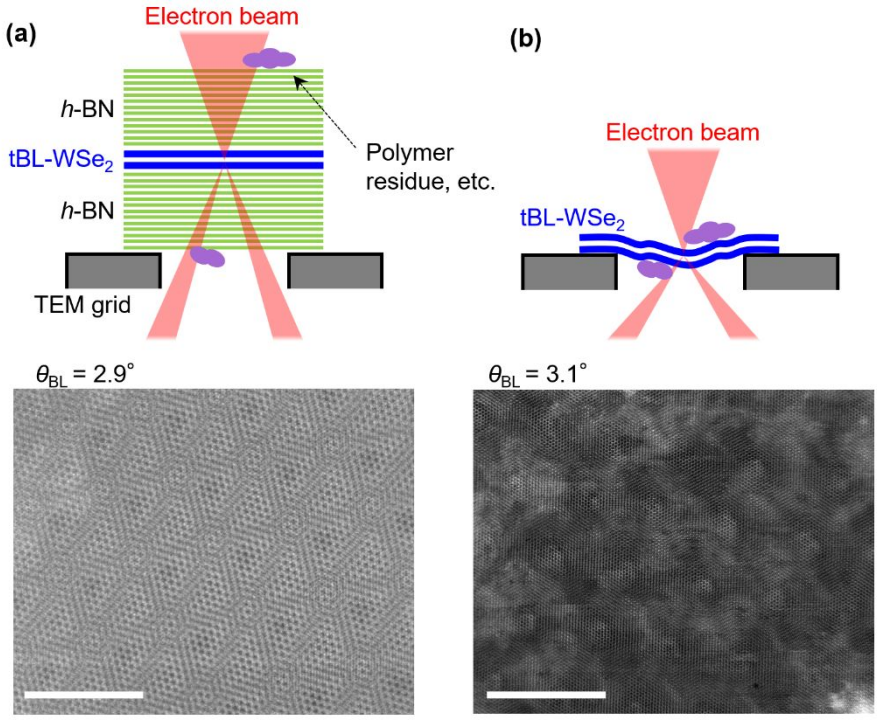

Fig. 4 Sample structure (top panels) and STEM image (bottom panels) of different tBL-WSe_2 devices: (a) tBL-WSe_2 encapsulated with top and bottom *h*-BN and (b) non-encapsulated tBL-WSe_2. All scale bars are 10 nm.

Author Contributions

Kei Kinoshita: Conceptualization; Data curation; Formal analysis; Funding acquisition; Investigation; Project administration; Validation; Visualization; Writing – original draft; Writing – review & editing. **Yung-Chang Lin:** Data curation; Formal analysis; Funding acquisition; Investigation; Project administration; Validation; Writing – original draft; Writing – review & editing. **Rai Moriya:** Conceptualization; Data curation; Formal analysis; Funding acquisition; Investigation; Project administration; Validation; Visualization; Writing – original draft; Writing – review & editing. **Shota Okazaki:** Resources. **Momoko Onodera:** Funding acquisition; Resources. **Yijin Zhang:** Funding acquisition; Project administration; Validation. **Ryosuke Senga:** Funding acquisition; Resources. **Kenji Watanabe:** Funding acquisition; Resources. **Takashi Taniguchi:** Resources. **Takao Sasagawa:** Funding acquisition; Resources. **Kazu Suenaga:** Funding acquisition; Project administration; Supervision. **Tomoki Machida:** Conceptualization; Funding acquisition; Project administration; Supervision; Validation; Visualization; Writing – original draft; Writing – review & editing.

Conflicts of interest

There are no conflicts of interest to declare.

Acknowledgements

This work was supported by JST-CREST, JST-Mirai, and JST-PRESTO (Grant Numbers JPMJCR15F3, JPMJCR1993, JPMJCR20B1, JPMJCR20B4, JPMJCR20B5, JPMJPR20L5, JPMJPR2009); JSPS KAKENHI (Grants Numbers JP21H04652, JP21H05232, JP21H05233, JP21H05234, JP21H05235, JP21H05236, JP21K18181, JP22H01898, JP22H05478, JP22K18317, JP22J22105, JP22KJ1104, JP23H00277, JP24K16991); and Support Center for Advanced Telecommunications Technology Research Foundation.

References

1. Y. Cao, V. Fatemi, A. Demir, S. Fang, S. L. Tomarken, J. Y. Luo, J. D. Sanchez-Yamagishi, K. Watanabe, T. Taniguchi, E. Kaxiras, R. C. Ashoori and P. Jarillo-Herrero, *Nature*, 2018, **556**, 80-84.
2. L. Wang, E.-M. Shih, A. Ghiotto, L. Xian, D. A. Rhodes, C. Tan, M. Claassen, D. M. Kennes, Y. Bai, B. Kim, K. Watanabe, T. Taniguchi, X. Zhu, J. Hone, A. Rubio, A. N. Pasupathy and C. R. Dean, *Nat. Mater.*, 2020, **19**, 861-866.
3. Y. Cao, V. Fatemi, S. Fang, K. Watanabe, T. Taniguchi, E. Kaxiras and P. Jarillo-Herrero, *Nature*, 2018, **556**, 43-50.
4. K. P. Nuckolls, M. Oh, D. Wong, B. Lian, K. Watanabe, T. Taniguchi, B. A. Bernevig and A. Yazdani, *Nature*, 2020, **588**, 610-615.
5. Y. Xie, A. T. Pierce, J. M. Park, D. E. Parker, E. Khalaf, P. Ledwith, Y. Cao, S. H. Lee, S. Chen, P. R. Forrester, K. Watanabe, T. Taniguchi, A. Vishwanath, P. Jarillo-Herrero and A. Yacoby, *Nature*, 2021, **600**, 439-443.
6. J. Cai, E. Anderson, C. Wang, X. Zhang, X. Liu, W. Holtzmann, Y. Zhang, F. Fan, T. Taniguchi, K. Watanabe, Y. Ran, T. Cao, L. Fu, D. Xiao, W. Yao and X. Xu, *Nature*, 2023, **622**, 63-68.
7. Y. Zeng, Z. Xia, K. Kang, J. Zhu, P. Knüppel, C. Vaswani, K. Watanabe, T. Taniguchi, K. F. Mak and J. Shan, *Nature*, 2023, **622**, 69-73.
8. K. L. Seyler, P. Rivera, H. Yu, N. P. Wilson, E. L. Ray, D. G. Mandrus, J. Yan, W. Yao and X. Xu, *Nature*, 2019, **567**, 66-70.
9. K. Tran, G. Moody, F. Wu, X. Lu, J. Choi, K. Kim, A. Rai, D. A. Sanchez, J. Quan, A. Singh, J. Embley, A. Zepeda, M. Campbell, T. Autry, T. Taniguchi, K. Watanabe, N. Lu, S. K. Banerjee, K. L. Silverman, S. Kim, E. Tutuc, L. Yang, A. H. MacDonald and X. Li, *Nature*, 2019, **567**, 71-75.
10. C. Jin, E. C. Regan, A. Yan, M. Iqbal Bakti Utama, D. Wang, S. Zhao, Y. Qin, S. Yang, Z. Zheng, S. Shi, K. Watanabe, T. Taniguchi, S. Tongay, A. Zettl and F. Wang, *Nature*, 2019, **567**, 76-80.
11. E. M. Alexeev, D. A. Ruiz-Tijerina, M. Danovich, M. J. Hamer, D. J. Terry, P. K. Nayak, S. Ahn, S. Pak, J. Lee, J. I. Sohn, M. R. Molas, M. Koperski, K. Watanabe, T. Taniguchi, K. S. Novoselov, R. V. Gorbachev, H. S. Shin, V. I. Fal'ko and A. I. Tartakovskii, *Nature*, 2019, **567**, 81-86.
12. X. Wang, K. Yasuda, Y. Zhang, S. Liu, K. Watanabe, T. Taniguchi, J. Hone, L. Fu and P. Jarillo-Herrero, *Nat. Nanotechnol.*, 2022, **17**, 367-371.
13. F. Ferreira, V. V. Enaldiev, V. I. Fal'ko and S. J. Magorrian, *Sci. Rep.*, 2021, **11**, 13422.
14. H. Yoo, R. Engelke, S. Carr, S. Fang, K. Zhang, P. Cazeaux, S. H. Sung, R. Hovden, A. W. Tsen, T. Taniguchi, K. Watanabe, G.-C. Yi, M. Kim, M. Luskin, E. B. Tadmor, E. Kaxiras and P. Kim, *Nat. Mater.*, 2019, **18**, 448-453.

15. A. Kerelsky, L. J. McGilly, D. M. Kennes, L. Xian, M. Yankowitz, S. Chen, K. Watanabe, T. Taniguchi, J. Hone, C. Dean, A. Rubio and A. N. Pasupathy, *Nature*, 2019, **572**, 95-100.
16. A. Weston, Y. Zou, V. Enaldiev, A. Summerfield, N. Clark, V. Zólyomi, A. Graham, C. Yelgel, S. Magorrian, M. Zhou, J. Zultak, D. Hopkinson, A. Barinov, T. H. Bointon, A. Kretinin, N. R. Wilson, P. H. Beton, V. I. Fal'ko, S. J. Haigh and R. Gorbachev, *Nat. Nanotechnol.*, 2020, **15**, 592-597.
17. M. Van Winkle, I. M. Craig, S. Carr, M. Dandu, K. C. Bustillo, J. Ciston, C. Ophus, T. Taniguchi, K. Watanabe, A. Raja, S. M. Griffin and D. K. Bediako, *Nat. Commun.*, 2023, **14**, 2989.
18. J. H. Baek, H. G. Kim, S. Y. Lim, S. C. Hong, Y. Chang, H. Ryu, Y. Jung, H. Jang, J. Kim, Y. Zhang, K. Watanabe, T. Taniguchi, P. Y. Huang, H. Cheong, M. Kim and G. H. Lee, *Nat. Mater.*, 2023, **22**, 1463-1469.
19. C. Zhang, C.-P. Chuu, X. Ren, M.-Y. Li, L.-J. Li, C. Jin, M.-Y. Chou and C.-K. Shih, *Sci. Adv.*, 2017, **3**, e1601459.
20. M. R. Rosenberger, H.-J. Chuang, M. Phillips, V. P. Oleshko, K. M. McCreary, S. V. Sivaram, C. S. Hellberg and B. T. Jonker, *ACS nano*, 2020, **14**, 4550-4558.
21. Y. Zhang, J.-H. Baek, C.-H. Lee, Y. Jung, S. C. Hong, G. Nolan, K. Watanabe, T. Taniguchi, G.-H. Lee and P. Y. Huang, *Sci. Adv.*, 2024, **10**, eadk1874.
22. L. J. McGilly, A. Kerelsky, N. R. Finney, K. Shapovalov, E. M. Shih, A. Ghiotto, Y. Zeng, S. L. Moore, W. Wu, Y. Bai, K. Watanabe, T. Taniguchi, M. Stengel, L. Zhou, J. Hone, X. Zhu, D. N. Basov, C. Dean, C. E. Dreyer and A. N. Pasupathy, *Nat. Nanotechnol.*, 2020, **15**, 580-584.
23. Z. Zhang, Y. Wang, K. Watanabe, T. Taniguchi, K. Ueno, E. Tutuc and B. J. LeRoy, *Nat. Phys.*, 2020, **16**, 1093-1096.
24. E. Li, J.-X. Hu, X. Feng, Z. Zhou, L. An, K. T. Law, N. Wang and N. Lin, *Nat. Commun.*, 2021, **12**, 5601.
25. Y.-C. Lin, A. Motoyama, P. Solís-Fernández, R. Matsumoto, H. Ago and K. Suenaga, *Nano Lett.*, 2021, **21**, 10386-10391.
26. N. N. Nam and M. Koshino, *Phys. Rev. B*, 2017, **96**, 075311.
27. S. Carr, D. Massatt, S. B. Torrisi, P. Cazeaux, M. Luskin and E. Kaxiras, *Phys. Rev. B*, 2018, **98**, 224102.
28. D. G. Purdie, N. Pugno, T. Taniguchi, K. Watanabe, A. Ferrari and A. Lombardo, *Nat. Commun.*, 2018, **9**, 5387.
29. M. Onodera, S. Masubuchi, R. Moriya and T. Machida, *Jpn. J. Appl. Phys.*, 2020, **59**, 010101.
30. K. Kim, M. Yankowitz, B. Fallahazad, S. Kang, H. C. Movva, S. Huang, S. Larentis, C. M. Corbet, T. Taniguchi, K. Watanabe, S. K. Banerjee, B. J. LeRoy and E. Tutuc, *Nano Lett.*, 2016, **16**, 1989-1995.
31. P. K. Poddar, Y. Zhong, A. J. Mannix, F. Mujid, J. Yu, C. Liang, J.-H. Kang, M. Lee, S. Xie and J. Park, *Nano Lett.*, 2022, **22**, 726-732.

32. Y.-C. Lin, C.-C. Lu, C.-H. Yeh, C. Jin, K. Suenaga and P.-W. Chiu, *Nano Lett.*, 2012, **12**, 414-419.
33. J. Kim, E. Ko, J. Jo, M. Kim, H. Yoo, Y. W. Son and H. Cheong, *Nat. Mater.*, 2022, **21**, 890-895.
34. V. V. Enaldiev, V. Zólyomi, C. Yelgel, S. J. Magorrian and V. I. Fal'ko, *Phys. Rev. Lett.*, 2020, **124**.
35. C. R. Dean, A. F. Young, I. Meric, C. Lee, L. Wang, S. Sorgenfrei, K. Watanabe, T. Taniguchi, P. Kim, K. L. Shepard and J. Hone, *Nat. Nanotechnol.*, 2010, **5**, 722-726.
36. L. Britnell, R. V. Gorbachev, R. Jalil, B. D. Belle, F. Schedin, A. Mishchenko, T. Georgiou, M. I. Katsnelson, L. Eaves, S. V. Morozov, N. M. Peres, J. Leist, A. K. Geim, K. S. Novoselov and L. A. Ponomarenko, *Science*, 2012, **335**, 947-950.
37. D. Rhodes, S. H. Chae, R. Ribeiro-Palau and J. Hone, *Nat. Mater.*, 2019, **18**, 541-549.
38. K. Kinoshita, R. Moriya, S. Okazaki, Y. Zhang, S. Masubuchi, K. Watanabe, T. Taniguchi, T. Sasagawa and T. Machida, *Nano Lett.*, 2022, **22**, 4640-4645.
39. K. Kinoshita, R. Moriya, S. Okazaki, Y. Zhang, S. Masubuchi, K. Watanabe, T. Taniguchi, T. Sasagawa and T. Machida, *Phys. Rev. Research*, 2023, **5**, 043292.
40. S. J. Magorrian, V. V. Enaldiev, V. Zolyomi, F. Ferreira, V. I. Fal'ko and D. A. Ruiz-Tijerina, *Phys. Rev. B*, 2021, **104**, 125440.
41. M. A. Kaliteevski, V. Enaldiev and V. I. Fal'ko, *Nano Lett.*, 2023, **23**, 8875-8880.
42. K. Momma and F. Izumi, *J. Appl. Cryst.*, 2011, **44**, 1272-1276.